Chaos, Solitons and Fractals 204 (2026) 117734

Contents lists available at ScienceDirect

Chaos, Solitons and Fractals

journal homepage: www.elsevier.com/locate/chaos

Unidirectional dynamics in translationally coupled bistable systems: Waves, fronts, and self-organization

Diego Molina C. [a,*], René G. Rojas [a], Marcel G. Clerc [b,1], Alejandro O. Leon [c]

[a] Instituto de Física, Pontificia Universidad Católica de Valparaíso, Casilla 4059, Chile
[b] Departamento de Física and Millennium Institute for Research in Optics, Facultad de Ciencias Físicas y Matemáticas, Universidad de Chile, Casilla 487-3, Santiago, Chile
[c] Departamento de Física, Facultad de Ciencias Naturales, Matemática y del Medio Ambiente, Universidad Tecnológica Metropolitana, Las Palmeras 3360, Ñuñoa 780-0003, Santiago, Chile

ARTICLE INFO

Keywords:
Translational coupling
Reaction-diffusion systems
Nonreciprocal waves
Nonreciprocal front propagation

ABSTRACT

Translational coupling takes place when the dynamics of a state variable at a given position depend on the state variable at a translated position, as occurs in optical experiments that present misaligned feedback. This article investigates analytically and numerically the effects of translational coupling on the dynamics of a spatially extended dissipative ϕ^4 system. We predict a translational-coupling-induced Andronov–Hopf instability with non-zero wavenumber. The resulting unidirectional waves are characterized using a Ginzburg–Landau equation. The analytic solution for this wave shows excellent agreement with the numerical results. For larger values of the coupling parameter, secondary instabilities occur, resulting in spatiotemporal chaotic dynamics. Beyond the dynamics of uniform equilibria and waves, this system exhibits fronts with nonreciprocal propagation. The front speed as a function of the translational coupling parameter is obtained by analytical approximations and numerical simulations, showing good agreement between the two methods. Increasing the translational coupling values, the domains at each side of the front core exhibit a rich self-organization that goes from regular to chaotic waves. Finally, numerical bifurcation diagrams are presented.

1. Introduction

When driving mechanisms counterbalance energy losses, macroscopic systems can exhibit a variety of responses, including nonlinear waves, fronts, complex oscillations, and localized structures [1–6]. These paradigmatic examples of robust phenomena exhibit universal features even if emerging in very different physical settings, such as mechanical [7–10], magnetic [11–14], and optical [15–18] systems. This article focuses on *dissipative waves* and *fronts*. The first state typically results from an Andronov–Hopf instability with non-zero wavenumber of a homogeneous stationary state [19], where the wave number and frequency depend on the parameters of the system. Furthermore, the wave amplitude reflects the competition between energy injection and dissipation, as typically accounted for by the Ginzburg–Landau equation [20]. Fronts [1], or domain walls, are another self-organization phenomenon, corresponding to the frontier separating two domains with different equilibria [20]. While fronts are spatially extended objects, in most instances, their core behaves as particle-type solutions [1,21,22]. Fronts are particularly promising for technological

* Corresponding author.
E-mail address: diego.molina.c@pucv.cl (Diego Molina C.).

[1] Given his role as Section Editor, Marcel Clerc had no involvement in the peer-review of this article and has no access to information regarding its peer-review. Full responsibility for the editorial process for this article was delegated to another journal editor.

https://doi.org/10.1016/j.chaos.2025.117734
Received 15 September 2025; Received in revised form 25 November 2025; Accepted 4 December 2025

applications, such as magnetic systems at the nanoscale [23] or driven optical media [24], where localized states can be information carriers. Domain walls naturally propagate when one of the domains is stable and the other is unstable, resulting in the invasion of the stable domain [25]. An extensive characterization of these fronts, along with the propagation mechanisms in terms of front pulling and pushing, is available in the literature [1]. Another case is that of fronts connecting stable states, or bistable fronts, where domain-wall propagation occurs if there is an energy difference between domains, resulting in the invasion of the energetically favorable state [26,27]. Several bistable models have been employed to characterize this dissipative self-organization [1].

Beyond characterizing waves and fronts, the control of their propagation via engineering coupling mechanisms is a central focus in the study of non-equilibrium systems [28–31]. While most studies focus on local interactions [32], this article considers the less-explored *translational coupling*. An experimental example of translational coupling is a liquid-crystal light valve with optical feedback, where a light beam can excite a liquid crystal layer and be re-injected with a lateral displacement. In systems with translational coupling, the evolution of the state variable $u(x,t)$, at the space and time coordinates x and t, depends on $u(x-L,t)$, i.e., u interacts with itself after a translation parameterized by the externally tunable control parameter L [33–36].

This article studies the effect of translational coupling in waves and fronts, and it is organized as follows. Our motivations are to study translational coupling in a reaction–diffusion-type model, which has not been investigated before; we also aim at predicting the emergence of complex wave and front dynamics in systems with translational coupling. In Section 2, we propose a reaction–diffusion-type model with bistability and translational coupling and solve its homogeneous stationary states in Section 3, finding an Andronov–Hopf instability. In Section 4, we use weakly nonlinear analysis to characterize the dynamics of the wave envelope, obtaining a Ginzburg–Landau equation. Comparisons of the analytic solution of this Ginzburg–Landau equation and the numerical results show excellent agreement. A secondary instability of the waves creates a complicated chaotic dynamics that we characterize numerically. In Section 5, we focus on front dynamics, and find analytically and numerically the translational-coupling-induced speed. As it occurs with the unidirectional waves, increasing the translational coupling parameter results in secondary instabilities that induce chaotic dynamics. Finally, in Section 6, we present our conclusions and remarks.

2. Model

Out-of-equilibrium systems exhibit multiple stable solutions. A simple equation displaying bistability is the ϕ^4-model. Let us start reviewing the dissipative ϕ^4-model, also known as the extended *Pitchfork normal form*, a paradigmatic reaction–diffusion equation with bistability and parity symmetry.

Consider a scalar real-valued field $u=u(x,t)$ that evolves according to the spatially extended Pitchfork normal form, which is a type of reaction diffusion equation [2]

$$\partial_t u = \epsilon u - u^3 + D\partial_{xx}u, \tag{1}$$

where ∂_t and ∂_{xx} are the temporal partial derivative and the Laplacian operator, respectively, and D is a diffusion constant. Reaction–diffusion equations describe many systems, including liquid-crystal light valves (see [28] and references therein), where $u(x,t)$ represents the average tilting angle of the liquid-crystal molecules with respect to a privileged axis.

In Eq. (1), there are three uniform *equilibria* (time-independent solutions), the simplest of them is $u_0^*=0$. Expanding around the u_0^* equilibrium, $u(x,t)=u_0^*+\delta u$, with $|\delta u|\ll 1$ being a small perturbation satisfying the linear equation

$$\partial_t u = \epsilon\delta u + D\partial_{xx}\delta u, \tag{2}$$

whose solution is

$$\delta u(x,t) = \sum_k A(k) e^{\left(\epsilon - Dk^2\right)t + ikx}, \tag{3}$$

where $A(k)$ is the initial-condition-dependent amplitude of the $k-$th mode. In Eq. (3), the time evolution of each Fourier mode depends on $\epsilon - Dk^2$. If there is at least one value of k such that $\epsilon - Dk^2 > 0$, then the perturbation grows exponentially and u_0^* is an unstable solution. On the other hand, if $\epsilon - Dk^2 < 0$ for all k, then the u_0^* attracts nearby orbits in the phase space. Since the uniform mode ($k=0$) has the largest growth rate, the $u_0^*=0$ is linearly stable if $\epsilon<0$, and linearly unstable for $\epsilon>0$. For $\epsilon>0$, two stable equilibria emerge, $u_\pm^*=\pm\sqrt{\epsilon}$. These states are connected by the $u\to -u$ symmetry of the system and correspond to the minima of the functional

$$V[u] = \int dx \left[-\frac{\epsilon u^2}{2} + \frac{u^4}{4} + \frac{D\left(\partial_x u\right)^2}{2} \right],$$

whose functional derivative, $\delta V/\delta u$, governs the dynamics of u via the relaxation equation

$$\partial_t u = -\frac{\delta V}{\delta u}. \tag{4}$$

For simplicity, model (1) does not include a so-called *imperfection parameter* η [37], which would break the $u\to -u$ symmetry, $\partial_t u = \eta + \epsilon u - u^3 + D\partial_{xx}u$. The presence of η would create an energy imbalance between the equilibria $u_\pm^*$, thereby obscuring the effects of translational coupling on the propagation of dissipative structures.

Eq. (1) exhibits solutions where the states $u_-^*=-\sqrt{\epsilon}$ and $u_+^*=\sqrt{\epsilon}$ inhabit in different domains separated by a front. This solution reads

$$u_{\text{Kink}}(x) = \sqrt{\epsilon}\tanh\left(\sqrt{\frac{\epsilon}{2D}}x\right), \tag{5}$$

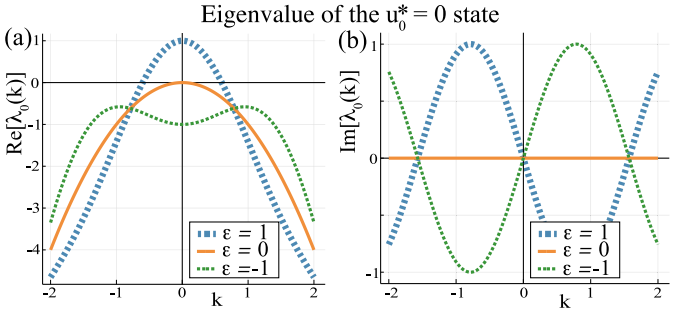

Fig. 1. Eigenvalue as a function of the wavenumber, $\lambda_0(k)$, of the $u_0^* = 0$ solution of Eq. (6), in the interval $-2 \le k \le 2$ for $L = 2$ and $D = 1$. The real part of the eigenvalue $\mathrm{Re}[\lambda_0(k)] = \epsilon \cos(kL) - Dk^2$ is negative for $\epsilon < 0$ but reaches a zero for $k = 0$ and $\epsilon = 0$. Further increasing ϵ results in larger positive $\lambda_0(0)$ values. The right panel shows the imaginary part of the eigenvalue, $\mathrm{Im}[\lambda_0(k)] = -i\epsilon \sin(kL)$. Note that $\mathrm{Im}[\lambda_0(0)] = 0$, indicating that the leading mode is stationary even if $L \neq 0$.

which is also known as *kink* solution. The kink satisfies $u_{\mathrm{Kink}} \to \pm\sqrt{\epsilon}$ for $x \to \pm\infty$. Given the $x \to -x$ symmetry, an anti-kink solution defined as $u_{\mathrm{Anti-Kink}}(x) = u_{\mathrm{Kink}}(-x)$ also exists.

2.1. Translational coupling

Let us introduce the translational coupling parameter L in the reaction part of Eq. (1),

$$\partial_t u(x,t) = \epsilon u(x-L,t) - u^3(x-L,t) + D\partial_{xx} u(x,t). \tag{6}$$

This equation preserves the $u \to -u$ symmetry of the Pitchfork normal form, but breaks $x \to -x$ invariance, producing nonreciprocal behaviors. For the sake of simplicity, the parameter L enters only in the reaction part of the equation. In contrast, the Laplacian represents local (nearest-neighbor) coupling due to, e.g., local transport governed by Fick's law.

The rest of this article is devoted to the systematic study of model Eq. (6) via analytical approximations and numerical methods. For the latter, Eq. (6) was integrated using finite differences for the spatial discretization and a fourth-order Runge–Kutta algorithm for the temporal evolution. Periodic and null-flux boundary conditions were employed for waves and fronts, respectively, in combination with a third-order extrapolation at the domain boundaries. The spatial and temporal step sizes used to discretize the system are $\Delta x = 0.1$ and $\Delta t = 0.005$.

3. Homogeneous stationary states

The values of the $u_0^* = 0$ and $u_\pm^* = \pm\sqrt{\epsilon}$ equilibria remain unaltered by L. However, their stability has to be inspected since Eq. (4) is no longer valid. Writing $u(x,t) = u_0^* + \delta u(x,t)$ with $|\delta u(x,t)| \ll 1$ being a small perturbation,

$$\partial_t \delta u(x,t) \approx \epsilon \delta u(x-L,t) + D\partial_{xx}\delta u(x,t), \tag{7}$$

whose solution reads $\delta u(x,t) = \sum_k A(k) e^{\lambda_0(k)t} e^{ikx}$. Here, the amplitude $A(k)$ depends on the initial conditions, and the eigenvalue function $\lambda_0(k) = \epsilon e^{-ikL} - Dk^2$ dictates the temporal evolution of the mode k. In Fig. 1, the eigenvalue is plotted as a function of k for three different values of ϵ, with $D = 1$ and $L = 2$. Near $\epsilon = 0$, the homogeneous ($k = 0$) mode has the largest real part of λ_0 and is fully controlled by the ϵ parameter, i.e., $\lambda_0(k = 0) = \epsilon$. Then, for small ϵ, the translational coupling does not alter the Pitchfork bifurcation diagram since the leading mode is uniform, $k = 0$, and non-oscillatory, $\mathrm{Im}[\lambda_0(k = 0)] = 0$, and the instability occurs simultaneously to the creation of the $u_\pm^*$ equilibria [37].

Let us consider now the $u_\pm^* = \pm\sqrt{\epsilon}$ equilibrium for $\epsilon > 0$. Writing Eq. (6) up to linear order in the small perturbation around $u_\pm^*$, $\delta u(x,t) \equiv u(x,t) - u_\pm^*$, we get

$$\partial_t \delta u(x,t) = -2\epsilon \delta u(x-L,t) + D\partial_{xx}\delta u(x,t), \tag{8}$$

where the corresponding eigenvalues, parameterized by k, are

$$\lambda_\pm(k) = -2\epsilon e^{-ikL} - Dk^2. \tag{9}$$

Fig. 2 shows the real and imaginary parts of $\lambda_\pm(k)$ for the $-2 \le k \le 2$ interval using $\epsilon = D = 1$. For relatively small L values, the thick segmented curve shows that $\mathrm{Re}[\lambda_\pm(k)] < 0$, and therefore the $u_\pm^*$ equilibria are stable. On the other hand, for the critical value $L = L_c \equiv 1.974$, there is an inhomogeneous mode with wave number k_c destabilizing the system, as revealed by the solid curve in Fig. 2(a). This leading mode has a characteristic angular frequency, $\omega_c = \mathrm{Im}[\lambda_\pm(k_c)] \neq 0$, as confirmed by Fig. 2(b). Further increasing L results in the temporal amplification of this leading mode (thinner segmented curve in Fig. 2).

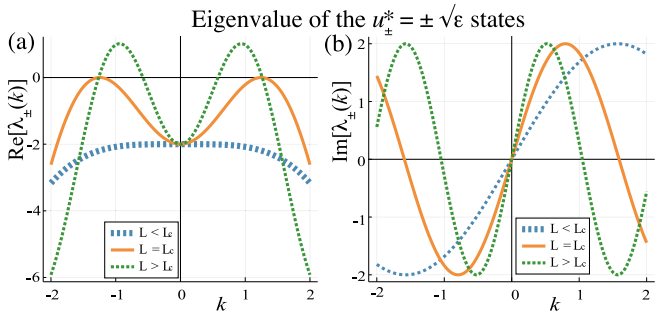

Fig. 2. Eigenvalue as a function of the wavenumber, $\lambda_\pm(-2 \le k \le 2)$, of $u_\pm^*$ of Eq. (6), for $\epsilon = D = 1$. (a) The real part of the eigenvalue $\lambda_\pm$, $\mathrm{Re}\left[\lambda_\pm(k)\right] = -2\epsilon\cos(kL) - Dk^2$, is negative for $L < L_c = 1.974$ (thick segmented curve) but reaches zero for $k = k_c$ and $L = L_c$ (solid curve). The thin segmented curve shows the eigenvalue for $L > L_c$. (b) Imaginary part of the eigenvalue function, $\mathrm{Im}\left[\lambda_\pm(k)\right] = 2\epsilon\sin(kL)$ that is zero for $k = 0$, indicating that the leading mode of the Pitchfork instability is stationary.

The critical mode ($k = k_c$) maximizes $\mathrm{Re}[\lambda_\pm(k)]$, or, equivalently,

$$\frac{\sin(k_c L)}{k_c L} = \frac{D}{\epsilon L^2}. \tag{10}$$

which is a transcendental equation with solution $k_c L = \pi$ for $D = 0$. For small but nonzero D, the approximate solutions for wave number (k_c) and angular frequency (ω_c) of the leading mode read

$$k_c(L) = \frac{3\pi}{2L} - \frac{\pi\sqrt{1 + 4D/\epsilon}}{2L^2}, \tag{11}$$

$$\omega_c(L) = 2\epsilon\sin\left(\frac{3\pi}{2} - \frac{\pi\sqrt{1 + 4D/\epsilon}}{2L}\right). \tag{12}$$

The next section will show that these formulas for $k_c(L)$ and $\omega_c(L)$ are in good agreement with their numerically obtained counterparts, even if D is as large as unity. At a fixed ϵ, there is a critical value of L for which the leading mode satisfies $\mathrm{Re}[\lambda_\pm(k_c; L = L_c)] = 0$, namely

$$L_c = 1.974\sqrt{\frac{D}{\epsilon}}, \tag{13}$$

which solves Eq. (10). This curve is plotted in Fig. 3(a) in the (ϵ, L) parameter space. For $L < L_c$, the $u_\pm^* = \pm\sqrt{\epsilon}$ states are stable, while they become unstable against unidirectional waves for $L > L_c$. Numerical simulations of Eq. (6) reveal that the instability of $u_\pm^* = \pm\sqrt{\epsilon}$ occurs in the ellipses in Fig. 3(a), showing excellent agreement with the analytic curve (ϵ, L_c). Furthermore, from Eq. (13), one can obtain the critical value ϵ for any given L, namely, $\epsilon_c = D(1.974/L)^2$. This indicates that the traditional Pitchfork bifurcation diagram is corrected due to the destabilization of the $u_\pm^* = \pm\sqrt{\epsilon}$ states for $\epsilon = \epsilon_c$, as shown in Fig. 3(b).

While the linear stability analysis is helpful to predict the Andronov–Hopf bifurcation with inhomogeneous critical mode, the resulting dynamics requires weakly nonlinear analysis, as done in the next section.

4. Unidirectional waves

Let us start considering the following Ansatz describing the waves emerging around $u_+^* = \sqrt{\epsilon}$

$$u(x,t) = \sqrt{\epsilon} + Ae^{i(k_c x + \omega_c t)} + \bar{A}e^{-i(k_c x + \omega_c t)} + W, \tag{14}$$

where the small amplitude $A = A(x,t)$ is a slowly-varying field, i.e., A satisfies $|\partial_t A| \ll |\omega_c A| \ll 1$ and $|\partial_x A| \ll |k_c A| \sim |A/L|$. $\bar{A}$ stands for the complex conjugate of A, and $W = W\left(A, \bar{A}, k_c x, \omega_c t\right)$ is a small correction expanded as

$$\begin{aligned} W =& C_{1,1}|A|^2 + C_{2,0}A^2(x,t)e^{2i(k_c x - \omega t)} \\ &+ C_{0,2}\bar{A}^2(x,t)e^{-2i(k_c x - \omega t)} + \cdots \end{aligned} \tag{15}$$

Replacing Eqs. (14) and (15) in Eq. (6), we get after straightforward but lengthy calculations

$$C_{1,1} = \frac{\mp 3}{\sqrt{\epsilon}}, \tag{16}$$

$$C_{2,0} = \frac{3\sqrt{\epsilon}e^{-2i(k_c L)}}{2i\omega_c + -2\epsilon e^{-2i(k_c L)} - 4Dk_c^2}, \tag{17}$$

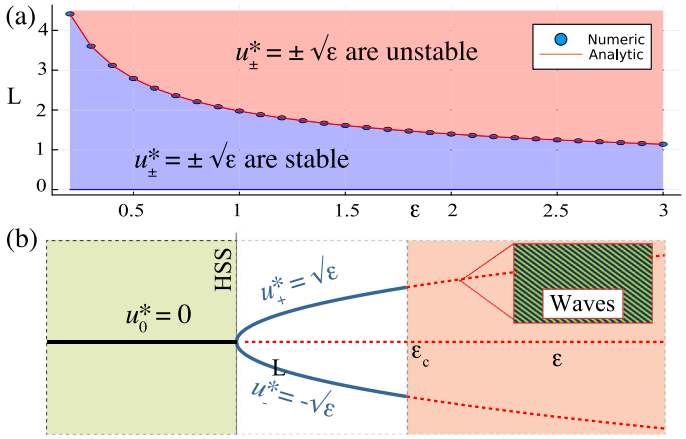

Fig. 3. Bifurcation diagrams of the homogeneous stationary states of model Eq. (6) for $D = 1$. (a) In the bluish and reddish regions, the $u^*_\pm = \pm\sqrt{\epsilon}$ states are stable and unstable, respectively. The separation is given by the analytic curve $L_c = 1.974\sqrt{D/\epsilon}$, or equivalently, $\epsilon_c = D\,(1.974/L)^2$, while the ellipsoids are the numerical results. (b) The bifurcation diagram of the Pitchfork transition for $L = 1.974$. While the destabilization of u^*_0, and the emergence of $u^*_\pm$, for $\epsilon = 0$ is well known, a secondary instability takes place for $\epsilon = \epsilon_c \equiv D\,(1.974/L)^2$. This is an Andronov–Hopf bifurcation of the $u^*_\pm$ states that gives rise to (unidirectionally) traveling waves, as shown in the inset.

with $C_{0,2}$ being the complex conjugate of $C_{2,0}$. On the other hand, the equation of A reads,

$$\partial_t A = \mu A - \tilde{c}A|A|^2 + 2ik_c D\partial_x A + D\partial_{xx} A, \tag{18}$$

with

$$\mu \equiv 2\epsilon k_c \Delta L \sin(k_c L_c) - 2\Delta\epsilon \cos(k_c L_c) \tag{19}$$

being the effective bifurcation parameter of this Andronov–Hopf instability, which depends on the $\Delta L \equiv L - L_c$ and $\Delta\epsilon \equiv \epsilon - \epsilon_c$ unfolding coefficients of the parameter space, i.e., μ indicates the transition between the bluish and reddish zones in Fig. 3(a). On the other hand,

$$\tilde{c} \equiv \frac{9\epsilon e^{-3i(k_c L)}}{i\omega_c - \epsilon e^{-2i(k_c L)} - 2Dk_c^2} - 15e^{-ik_c L} \tag{20}$$

is the complex coefficient of the cubic nonlinearity, accounting for the saturation, $c_r \equiv \mathrm{Re}[\tilde{c}] > 0$, and the frequency shift, $c_i \equiv \mathrm{Im}[\tilde{c}] > 0$. Finally, the terms $\propto \partial_{xx} A$ and $\propto i\partial_x A$ are diffusion and a phase gradient (wavenumber shift) by the translational coupling. The latter can be eliminated by a change of variables of the form $B = Ae^{-ik_c x}$, resulting in

$$\partial_t B = \left(\mu + Dk_c^2\right) B - \tilde{c}B|B|^2 + D\partial_{xx} B. \tag{21}$$

Eq. (18), or its equivalent form (21), corresponds to the Ginzburg–Landau equation [20], a paradigmatic model of nonlinear waves [1]. Beyond the $A = B = 0$ state, for $\mu > 0$, the simplest uniform solution of this amplitude equation reads

$$A(t) = \sqrt{\frac{\mu}{c_r}} \exp\left[i\left(\frac{\mu c_i}{c_r} t + \phi_0\right)\right], \tag{22}$$

where the phase ϕ_0 depends on the initial condition. This $A(t)$ solution is a unidirectional wave. Replacing Eq. (22) in Eq. (14), we get at dominant-order in μ

$$u(x,t) \approx \sqrt{\epsilon} + 2\sqrt{\frac{\mu}{c_r}} \cos\left(k_c x + \left[\omega_c - \frac{\mu c_i}{c_r}\right] t + \phi_0\right). \tag{23}$$

Note that Eq. (23) represents waves traveling only leftward for $L > 0$, that is, the Andronov–Hopf instability generates nonreciprocal wave propagation. If $L < 0$, the propagation direction reverses. On the other hand, the temporal oscillation in the wave amplitude, Eq. (22), is an angular frequency shift $\Delta\omega = -\mu c_i/c_r$ for the wave (23). The analytic wave number, angular frequency, and the modulus of the amplitude, $|A|$, are compared to their numerical counterparts in Fig. 4(a), (b), and (c), respectively, showing an excellent quantitative agreement for $|\Delta L| \ll 1$.

The largest Lyapunov exponent (LLE), λ_{LLE}, can be used as a numerical indicator to demonstrate the presence of chaos in this system, as illustrated in Fig. 4(d). The LLE was obtained by calculating the distance $\|\delta u_{\mathrm{LLE}}(t_{n+1})\|$ between two initially nearby trajectories at times $t_{n+1} = n\tau$, with $\tau = 5$ and $n = 0, \ldots, N$ for $N = 30$. Other τ and N values yield equivalent results. The notation $\|a\|$ stands for the euclidean norm of the discretized scalar field a, $\|a\| = \sqrt{\sum_{j=1}^{m} a^2\,(x_j)}$, with $x_j = j \cdot \Delta x$ being the positions in the

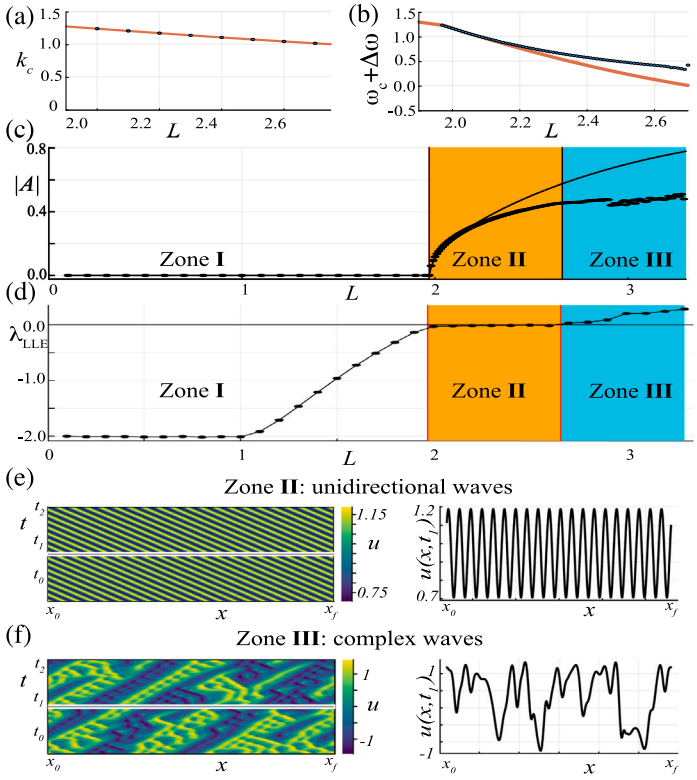

Fig. 4. Unidirectional waves by translational coupling. The panels (a) to (d) show the wave number k_c, angular frequency $\omega_c + \Delta\omega$, amplitude norm $|A|$, and largest Lyapunov exponent λ_{LLE}, respectively, as a function of L, using $D = \epsilon = 1$. (a) The solid curve shows the wave number of formula (11) and compares it with the numeric counterpart (ellipses), showing an excellent agreement for all the shown values of L. (b) The angular frequency is composed of a critical part given by the Andronov–Hopf instability, Eq. (12), and a correction from the solution of the Ginzburg–Landau equation (22). (c) and (d) show the modulus of the amplitude and the largest Lyapunov exponent (LLE) as a function of L, respectively. Three regions are distinguished: in Zone I, the $u_{\pm}^{*} = \pm\sqrt{\epsilon}$ states are stable and the wave amplitude decays to zero. This convergence $A \to 0$ implies a non-chaotic behavior, $\lambda_{\text{LLE}} < 0$. In Zone II, the wave amplitude grows and eventually saturates. At the onset of the instability, the amplitude obeys the $|A| \propto (L - L_c)^{1/2}$ power law, but eventually deviates from formula (22) and enters in Zone III for $L > L_{c2} = 2.61$, where chaos is observed. (e) and (f) show the spatiotemporal diagrams (left panels) and field profile at $t = t_1$ (right panels) for $L = 2.1$ (Zones II) and $L = 3.2$ (Zone III), respectively. Here, $x_0 = -50$, $x_f = 50$, $t_0 =$ is the transient time, $t_1 = t_0 + 50$, and $t_2 = t_0 + 100$.

discretized domain. Then, the LLE reads

$$\lambda_{\text{LLE}} \approx \frac{1}{t_N} \sum_{n=0}^{N} \ln\left(\frac{\|\delta u_{\text{LLE}}(t_{n+1})\|}{\|\delta u_{\text{LLE}}(t_n)\|} \right). \tag{24}$$

As Fig. 4 reveals, the $|A| = 0$ equilibrium is stable for $L < L_c$ (Zone I in the figure). The convergence to the $|A| = 0$ state corresponds to a $\lambda_{\text{LLE}} < 0$ as shown in Fig. 4(d). On the other hand, in Zone II, the wave grows as $|A| \propto \mu^{1/2}$ for $\mu > 0$. In Zone II, two solutions separated by a small ϕ_0 value, remain at the same distance $\|\delta u_{\text{LLE}}(t_{n+1})\|$ in the phase space, resulting in $\lambda_{\text{LLE}} \approx 0$. While in the first part of Zone II, the analytical approximation and numerical solutions for $|A|$ are in excellent agreement, the numeric value deviates as $\Delta = L - L_c$ grows, eventually entering in Zone III. In this region, $L > L_{c2} = 2.61$, complex spatiotemporal patterns are observed, which corresponds to a positive LLE, as shown in Fig. 4(d). To grasp this dynamics at the onset of this secondary bifurcation, Figs. 5(a) and 5(b) show the Fourier spectra of u, $|F[u]|$, for $L = 2.6 < L_{c2}$ and $L = 2.65 > L_{c2}$, respectively. As these plots show, a new Fourier peak emerges in the spectra for $L > L_{c2}$, creating aperiodic behaviors. The continuous growth of the LLE in Fig. 4(d) and the continuous growth of the non-resonant Fourier peaks as L is varied, indicate that the transition is of a supercritical type.

The transition from coherent to chaotic wave dynamics in our ϕ^4-model, Eq. (6), can be framed within the established theory of the Ginzburg–Landau equation [20]. In particular, the onset of irregular behavior is associated with secondary modulational instabilities of the plane-wave states predicted by the amplitude equation (21), giving rise to spatiotemporal intermittency and defect turbulence [20,35,38]. Then, even if translational coupling is a specific forcing mechanism, the observed chaotic regime can be identified with the spatiotemporal instability scenarios well established in the Ginzburg–Landau model [20].

So far, we have predicted and characterized the Andronov–Hopf instability with non-zero wavenumber that gives rise to unidirectionally traveling waves. An analytic expression for the wave solution is found using weakly nonlinear analysis, and it

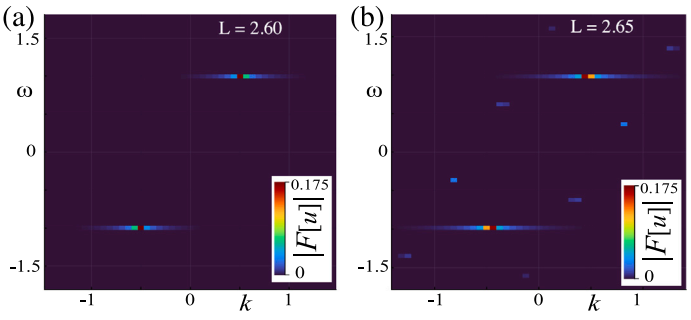

Fig. 5. Fourier spectra, $|F[u]|$, as a function of the wavenumber k and angular frequency ω at the onset of the secondary instability of the system. (a) For $L = 2.60 < L_{c2}$, the unidirectional wave has a clean Fourier spectrum. (b) For $L = 2.65 > L_{c2}$, new peaks emerge with incommensurable angular frequency and wave number.

shows excellent agreement with its numeric counterpart at the onset of the instability. Further increasing the translational coupling parameter results in the emergence of a new oscillatory mode, eventually leading to a chaotic solution. As we show in the next section, such a phenomenology is inherited by front solutions connecting the domains centered on the $\pm\sqrt{\epsilon}$ states.

5. Fronts

In infinite systems, single front solutions such as Eq. (5) obey $u_{\text{Kink}}(x \to \pm\infty) = \pm 1$, which does not occur in experimental setups. Correspondingly, in our finite simulation box, zero-flux boundary conditions were applied, and the field was extrapolated cubically at the borders to evaluate the $u(x-L,t)$ and $u^3(x-L,t)$ terms. The general phenomenology is presented in Fig. 6. For small values of L, the fronts connect $u_-^* = -\sqrt{\epsilon}$ and $u_+^* = \sqrt{\epsilon}$ and propagate at a constant speed, as shown in Fig. 6(a). To find the front speed analytically, we start writing Eq. (6) as $\partial_t u(x,t) = F(u(x-L,t)) + D\partial_{xx}u(x,t)$, and use the following Ansatz based on Eq. (5),

$$u(x,t) = u_{\text{Kink}}\left(x - x_F\right) + \widetilde{W}(x, x_F). \tag{25}$$

where $x_F = x_F(t)$ is the front position and $\widetilde{W}$ is a small correction emerging from the nonlinear nature of the system. Up to linear order in L,

$$\hat{L}\widetilde{W} = -v\partial_x u_{\text{Kink}}(x) + L\left(\frac{\partial F}{\partial u_{\text{Kink}}}\right)\partial_x u_{\text{Kink}}(x) \tag{26}$$

where $\hat{L} = \left(\partial F/\partial u_{\text{Kink}}\right) + D\partial_{xx}$, $v \equiv \partial_t x_F$ is the front speed, and the derivative $\left(\partial F/\partial u_{\text{Kink}}\right)$ is evaluated on $u_{\text{Kink}}(x)$. Using the inner product $(a,b) = \int_{-\infty}^{\infty}(a\cdot b)\,dx$, $\hat{L}$ is a self-adjoint operator, and the Fredholm alternative for Eq. (26) gives

$$v = L\frac{\int_{-\infty}^{\infty}\left(\frac{\partial F}{\partial u_{\text{Kink}}}\right)\left[\partial_x u_{\text{Kink}}(x)\right]^2 dx}{\int_{-\infty}^{\infty}\left[\partial_x u_{\text{Kink}}(x)\right]^2 dx} = \frac{2\epsilon L}{5}, \tag{27}$$

which is plotted in Fig. 6(a), displaying an excellent agreement with the numerical results (ellipsoids), even for L values close to unity. For larger values of the L control parameter, the system develops waves, as expected from the discussion of the previous section. The spatiotemporal diagram and the spatial profile of the solutions are shown in Fig. 6(b). For this figure, the initial condition is the kink-shaped function, formula (5), centered on $x_{F,0} \equiv x_F(0)$, that is $u(x, t=0) = u_{\text{Kink}}(x - x_{F,0})$. The dynamics of fronts are illustrated in the bifurcation diagram of Fig. 6(d) for the dynamical indicator $A^{(av)}$, which averages the oscillation amplitude at the right of the front. For small values of L (Zone I), the fronts move at the constant speed $v = 2\epsilon L/5$, and connect two uniform states. Since the front travels rightwards for $L > 0$, it perturbs the domain at its right, resulting in the waves discussed in Section 4 if L exceeds the Andronov–Hopf threshold. Note that in Zone II the fronts continue to advance steadily even if connecting nonuniform states. A further increase in L destabilizes the traveling waves, and in Zone III, the emergent chaotic oscillations eventually pin the front. These transitions can be understood using the Ginzburg–Landau equation (21) satisfied by each domain, which predicts waves undergoing secondary instabilities that lead to defect-mediated spatiotemporal chaos. Thus, while the translational coupling provides a system-specific mechanism for breaking parity, the complexity of the front solutions reflects the universal spatiotemporal regimes characteristic of Ginzburg–Landau dynamics. Then, in brief, while the front exhibits a complex zoology, it is fundamentally inherited from the wave dynamics discussed earlier.

Note that, while Fig. 6 shows the evolution of the system when it starts with a kink-shaped initial condition, it is also possible to start with a randomly perturbed initial condition $u(x, t=0) = u_{\text{Kink}}(x - x_{F,0}) + 10^{-3}\delta u(x)$, where $\delta u(x)$ is a random variable of mean zero and standard deviation one. The resulting dynamics are shown in Fig. 7(a) and (b), where the initial conditions are amplified temporally and permanently, respectively. In Fig. 7(a), for $L = 2.2$, the waves decay, while in (b), for $L = 2.4$, the left-side perturbation saturates to standing waves due to the boundary conditions.

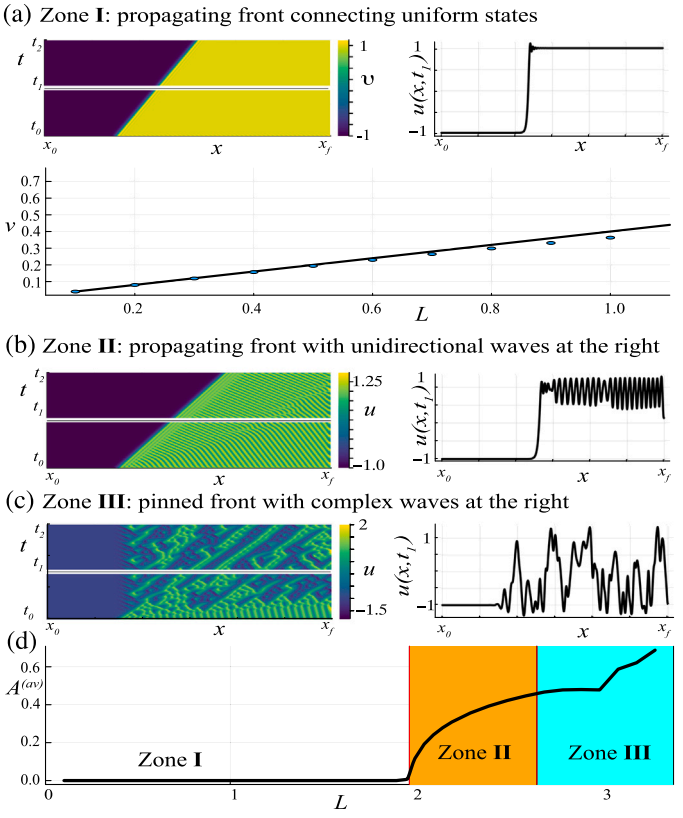

Fig. 6. Front dynamics. (a), (b), and (c) show the spatiotemporal diagrams (left panels) and field profiles (right panels) for $L = 1.7$ (Zone I), $L = 2.4$ (Zone II), and $L = 3.3$ (Zone III), with$x_0 = -150$, $x_f = 150$, $t_0 = 0$, $t_1 = 75$, and $t_2 = 150$. The temporal average value of the amplitude at the right of the front is plotted in (d). Three distinct behaviors can be observed: approximately monotonous fronts propagate in Zone I due to L; regular (Zone II) and chaotic (Zone III) waves emerge in the right domain. This zoology is inherited from the instabilities of the domain centered around $\sqrt{\epsilon}$, c.f. Fig. 4.

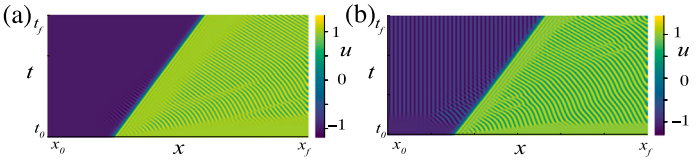

Fig. 7. Front propagation for (a) $L = 2.2$ and (b) $L = 2.4$. Here, $x_0 = -150$, $x_f = 150$, $t_0 =$ is the transient time, $t_1 = t_0 + 50$, and $t_f = 150$. The noisy initial condition here is a front solution plus a small random variable.

6. Conclusions

The phenomenology of dissipative waves and fronts is well-known in systems with local coupling. On the other hand, the *translational coupling*, where a field $u(x,t)$ at position x and time t couples to itself at a translated position $x - L$, $u(x - L, t)$, remains much less explored. This article studied systematically a dissipative ϕ^4–model, also known as the spatially extended Pitchfork normal form, with a translational coupling for the field $u(x,t)$,

$$\partial_t u(x,t) = \epsilon u(x - L, t) - u^3(x - L, t) + D\partial_{xx}u(x,t).$$

While the Pitchfork bifurcation of the $u_0^* = 0$ state at $\epsilon = 0$ is unaffected by L, the translational coupling modifies the stability of the $u_\pm^* = \pm\sqrt{\epsilon}$ equilibria. Indeed, at $L_c = 1.974\sqrt{D/\epsilon}$, an Andronov–Hopf bifurcation with non-zero wave number takes place. This instability gives rise to *unidirectional waves* since they travel leftward and rightward for $L > 0$ and $L < 0$, respectively. The linear stability analysis is done analytically and used to build a bifurcation diagram of the system in the two-dimensional parameter space (ϵ, L). Via weakly nonlinear analysis, we derived the Ginzburg–Landau equation for the wave envelope, providing an analytic solution for the wave amplitude, $A \propto \left(L - L_c\right)^{1/2}$. While the model preserves the $u \to -u$ symmetry, the translational coupling breaks

the $x \to -x$ invariance, resulting in a phase gradient in the amplitude equation ($i\partial_x A$). Further increasing L results in a secondary instability, where the waves are chaotic and display complex spatiotemporal diagrams. Indeed, one can distinguish three regions: in Zone I ($L < L_c$), the waves decay and the system converges to its homogeneous stationary solution $A \to 0$, showing a negative largest Lyapunov exponent ($\lambda_{\mathrm{LLE}} < 0$). In Zone II ($L \gtrsim L_c$), the waves exhibit a finite amplitude and travel leftwards with $\lambda_{\mathrm{LLE}} \approx 0$. Finally, in Zone III, the waves are chaotic as demonstrated by a positive LLE.

We also study the translational-coupling-induced dynamics of *fronts* connecting the $u_-^* = -\sqrt{\epsilon}$ and $u_+^* = \sqrt{\epsilon}$ states at the left and the right of the front, respectively. The fronts propagate with a speed proportional to the translational coupling parameter, $v \propto L$, that we obtain analytically and numerically, finding an excellent agreement between the two approaches. As L increases, the front connects a uniform state (at the left of the front) with a region of waves (at the right of the front), which eventually becomes chaotic for large L. As a result of this transition to complex waves, the front becomes pinned. A bifurcation diagram for the front dynamics is presented, distinguishing the three regimes mentioned earlier. We find that the spatiotemporal dynamics of fronts originate from the instabilities of the connected states ($u_+^* = \sqrt{\epsilon}$ if $L > 0$).

As a final remark, translational coupling emerges as a versatile route to rich nonequilibrium behavior. In this study, we analytically predicted, characterized, and numerically confirmed the onset of unidirectional waves and propagating fronts. Given the dynamical complexity of systems with translational coupling, our model considers simplifications, such as the independence of the diffusion constant and the translational coupling parameter. Consequently, although our results could be applied to experiments with liquid crystal light valves with optical feedback, in order to describe the experimental observations more quantitatively than qualitatively, it is necessary to incorporate locally dependent linear terms, as well as the effects of inherent fluctuations (noise), into the model Eq. (6). The study of the experimental dynamics of the fronts is currently under development. V

CRediT authorship contribution statement

Diego Molina C.: Visualization, Software, Investigation, Formal analysis, Conceptualization. **René G. Rojas:** Writing – review & editing, Validation, Supervision, Methodology, Formal analysis, Conceptualization. **Marcel G. Clerc:** Writing – review & editing, Validation, Supervision, Methodology, Formal analysis. **Alejandro O. Leon:** Writing – review & editing, Writing – original draft, Validation, Supervision, Methodology, Funding acquisition, Formal analysis.

Declaration of competing interest

The authors declare that they have no known competing financial interests or personal relationships that could have appeared to influence the work reported in this paper.

Acknowledgments

We thank Juan Marín-Medina for fruitful discussions, and gratefully acknowledge financial support in Chile from FONDECYT, Chile Grant 11230120, and 1252227. MGC acknowledges the financial support of ANID Millennium Science Initiative Program-ICN17_012.

Data availability

Data will be made available on request.

References

[1] Pismen LM. Patterns and interfaces in dissipative dynamics. Berlin: Springer; 2006.
[2] Hoyle RB. Pattern formation: an introduction to methods. Cambridge: Cambridge University Press; 2006.
[3] Murray JD. Mathematical biology I and II. New York: Springer-Verlag; 2001.
[4] Cross M, Greenside H. Pattern formation and dynamics in nonequilibrium systems. New York: Cambridge University Press; 2009.
[5] Scott A. Encyclopedia of nonlinear science. New Yor: Routledge; 2006.
[6] Ostrovsky L, Pelinovsky E, Shrira V, Stepanyants Y. Localized wave structures: Solitons and beyond. Chaos 2024;34:062101.
[7] Cho H, Yu MF, Vakakis AF, Bergman LA, McFarland MD. Tunable, broadband nonlinear nanomechanical resonator. Nano Lett 2010;10:1793.
[8] Djorwé P, Pennec Y, Djafari-Rouhani B. Self-organized synchronization of mechanically coupled resonators based on optomechanics gain-loss balance. Phys Rev B 2020;102:155410.
[9] Martens EA, Thutupalli S, Fourriere A, Hallatschek O. Chimera states in mechanical oscillator networks. Proc Natl Acad Sci USA 2013;110:10563.
[10] Deng B, Raney JR, Bertoldi K, Tournat V. Nonlinear waves in flexible mechanical metamaterials. J Appl Phys 2021;130:040901.
[11] Berrios-Caro E, Clerc MG, Ferre MA, Leon AO. Oscillating decorated interfaces in parametrically driven systems. Phys Rev E 2018;97:012207.
[12] Leon AO, Clerc MG, Altbir D. Dissipative magnetic breathers induced by time-modulated voltages. Phys Rev E 2018;98:062213.
[13] Cabanas AM, Clerc MG, Laroze D, Leon AO. Chaotic patterns and localized states in spin valves. J Magn Magn Mater 2019;476:589.
[14] Fattouhi M, Thiaville A, García-Sánchez F, Otxoa RM, Estévez MP García, Martínez E, López-Díaz L. Dissipative solitons signature in achiral Néel magnetic domain walls driven by spin–orbit torque. Commun Phys 2025;8:234.
[15] Brambilla M, Lugiato LA, Stefani M. Formation and control of localized structures in nonlinear optical systems. Chaos 1996;6:368.
[16] Arecchi FT, Boccaletti S, Ramazza P. Pattern formation and competition in nonlinear optics. Phys Rep 1999;318:1.
[17] Oppo GL, Yao AM, Cuozzo D. Self-organization, pattern formation, cavity solitons, and rogue waves in singly resonant optical parametric oscillators. Phys Rev A 2013;88:043813.

[18] Xu G, Nielsen AU, Garbin B, Hill L, Oppo GL, Fatome J, Murdoch SG, Coen S, Erkintalo M. Spontaneous symmetry breaking of dissipative optical solitons in a two-component Kerr resonator. Nat Commun 2021;12:4023.
[19] Andronov AA, Khajkin SE. Theory of oscillations. London: Dover; 1987.
[20] Aranson IS, Kramer L. The world of the complex Ginzburg–Landau equation. Rev Modern Phys 2002;74:99.
[21] Fisher RA. The wave of advance of advantageous genes. Ann Eugen 1937;7:335.
[22] Kolmogorov A, Petrovsky I, Piskunov N. Study of a diffusion equation that is related to the growth of a quality of matter and its application to a biological problem. Bull Univ Moskou Ser Int Se. 1937;7:1.
[23] Luo Z, Hrabec A, Dao TP, Sala G, Finizio S, Feng J, Mayr S, Raabe J, Gambardella P, Heyderman LJ. Current-driven magnetic domain-wall logic. Nature 2020;579:214.
[24] Hasegawa A. Soliton-based optical communications: an overview. IEEE J Sel Top Quantum Electron 2000;6:1161.
[25] Van Saarloos W. Front propagation into unstable states. Phys Rep 2003;386:29.
[26] Pomeau Y. Front motion, metastability and subcritical bifurcations in hydrodynamics. Phys D 1986;23:3.
[27] Clerc MG, Nagaya T, Petrossian A, Residori S, Riera CS. First-order Fréedericksz transition and front propagation in a liquid crystal light valve with feedback. Eur Phys J D 2004;28:435.
[28] Aguilera-Rojas PJ, Alfaro-Bittner K, Clerc MG, Díaz-Zúñiga M, Moya A, Pinto-Ramos D, Rojas RG. Nonlinear wave propagation in a bistable optical chain with nonreciprocal coupling. Commun Phys 2024;7:195.
[29] Alekseeva LV, Povkh IV, Stroganov VI, Kidyarov BI, Pasko PG and. A nonreciprocal optical element. J Opt Technol 2003;70:525.
[30] Mirza IM, Ge W, Jing H. Optical nonreciprocity and slow light in coupled spinning optomechanical resonators. Opt Expr 2019;27:25515.
[31] Yang P, Xia X, He H, Li S, Han X, Zhang P, Li G, Zhang P, Xu J, Yang Y, Zhang T. Realization of nonlinear optical nonreciprocity on a few-photon level based on atoms strongly coupled to an asymmetric cavity. Phys Rev Lett 2019;123:233604.
[32] Collet P, Eckmann JP. Instabilities and fronts in extended systems. Princeton: Princeton University Press; 1990.
[33] del Campo F, Haudin F, Rojas RG, Bortolozzo U, Clerc MG, Residori S. Effects of translational coupling on dissipative localized states. Phys Rev E 2012;86:036201.
[34] Clerc MG, Coulibaly S, Campo Fdel, Garcia-Nustes MA, Louvergneaux E, Wilson M. Recurrent noise-induced phase singularities in drifting patterns. Phys Rev E 2015;92. 050902(R).
[35] Alvarez-Garrido F, Clerc MG, Gonzalez-Cortes G. Transition to spatiotemporal intermittency and defect turbulence in systems under translational coupling. Phys Rev Lett 2020;124:164101.
[36] Haudin F, Rojas RG, Bortolozzo U, Clerc MG, Residori S. Vortex emission accompanies the advection of optical localized structures. Phys Rev Lett 2011;106:063901.
[37] Strogatz SH. Nonlinear dynamics and chaos: with applications to physics, biology, chemistry, and engineering. CRC Press; 2018.
[38] Chate H. Spatiotemporal intermittency regimes of the one-dimensional complex Ginzburg–Landau equation. Nonlinearity 1994;7:185.